

Charge-Density-Wave Oscillator Networks for Solving Combinatorial Optimization Problems

Jonas Olivier Brown^{1,2†}, Taosha Guo^{3†}, Fabio Pasqualetti^{3*},
and Alexander A. Balandin^{1,2,4*}

¹Department of Materials Science and Engineering, University of California, Los Angeles, 90095, California, USA.

²California NanoSystems Institute, University of California, Los Angeles, 90095, California, USA.

³Department of Mechanical Engineering, University of California, Riverside, 92507, California, USA.

⁴Center for Quantum Science and Engineering, University of California, Los Angeles, 90095, California, USA.

*Corresponding author(s). E-mail(s): fabiopas@ucr.edu;
balandin@seas.ucla.edu;

Contributing authors: jonasbrown@ucla.edu; tguo023@ucr.edu;

[†]These authors contributed equally to this work.

Abstract

Many combinatorial optimization problems fall into the non-polynomial time NP-hard complexity class, characterized by computational demands that increase exponentially with the size of the problem in the worst case. Solving large-scale combinatorial optimization problems efficiently requires novel hardware solutions beyond the conventional von Neumann architecture. We propose an approach for solving a type of NP-hard problem based on coupled oscillator networks implemented with charge-density-wave condensate devices. Our prototype hardware, based on the $1T$ polymorph of TaS_2 , reveals the switching between the charge-density-wave electron-phonon condensate phases, enabling room-temperature operation of the network. The oscillator operation relies on hysteresis in current-voltage characteristics and bistability triggered by applied electrical bias. This work presents a network of injection-locked, coupled oscillators whose phase dynamics follow the Kuramoto model and demonstrates that such coupled quantum oscillators naturally evolve to a ground state capable of solving combinatorial optimization problems. The coupled oscillators based on charge-density-wave

condensate phases can efficiently solve NP-hard Max-Cut benchmark problems, offering advantages over other leading oscillator-based approaches. The nature of the transitions between the charge-density-wave phases, distinctively different from resistive switching, creates the potential for low-power operation and compatibility with conventional Si technology.

Keywords: charge-density-waves, quantum materials, coupled oscillators, Max-Cut, NP-hard optimization.

The limitations of Moore’s law and rising energy demands in AI training have driven the development of unconventional computing methods to efficiently solve combinatorial optimization problems—common in real-world applications like routing, scheduling, and telecommunications—which can be mapped into Ising models [1, 2]. Such problems belong to the NP-hard or NP-complete complexity classes. Finding the ground states of Ising models using digital computers requires exponentially growing resources as the problem size increases, making it difficult to solve even problems of moderate size efficiently. Solving the Ising model efficiently requires novel hardware computation paradigms beyond conventional von Neumann architecture [3, 4]. Ising machines offer a promising approach to addressing complex and time-consuming optimization problems using traditional digital computing methods and algorithms [5–8]. Ising machines have been proposed on various technological platforms, including quantum-based systems like adiabatic quantum computing and quantum annealing using superconducting qubits [9–14], CMOS-based systems such as digital and mixed-signal CMOS annealers [15–18], and optical systems utilizing coherent networks of degenerate optical parametric oscillators [19–21]. While these approaches show potential, they face significant challenges. Quantum annealers incur high operational costs and require complex cryogenic environments. Digital CMOS annealers struggle to maintain true randomness and require substantial post-processing. Optical coherent Ising machines (CIM) need long fiber ring cavities for temporal multiplexing and rely on power-intensive field-programmable gate arrays FPGAs for coupling. Annealing, quantum solutions, and dynamical system solvers are three approaches to addressing complex optimization problems. Simulated annealing (SA) has broad applicability, extending beyond Ising models to a wide range of optimization problems. However, it can be trapped in local optima, especially in complex energy landscapes, and requires many iterations to find the global minimum [22]. Quantum solutions and dynamical system solvers use parallelism to explore multiple solutions simultaneously. Quantum entanglement enables quantum systems to navigate the energy landscape more efficiently. However, current quantum devices have limited qubit counts and are prone to errors, scalability issues, problems with generalizing to other optimization problems, and require complex cryogenic environments, leading to high operational costs [9, 12]. Dynamical system solvers deliver fast convergence, scale efficiently, and run on various hardware platforms. However, effectiveness can vary depending on the specific structure of the problem. In contrast, to slow annealing methods that maintain thermal equilibrium or ground state conditions, faster dynamical system approaches such as

those using coherent Ising machines (CIMs) [19] or coupled oscillators [7, 23–29] drive the system toward the lowest energy state of the Ising model [1, 2]. Optical CIMs require long fiber optic cables to process multiple signals over time and rely on power-intensive field-programmable gate arrays (FPGAs) for coupling, limiting scaling, and power efficiency [19]. Recent studies [6, 30, 31] have demonstrated the feasibility of using coupled oscillator networks to solve large-scale Ising problems. Experimentally, coupled electronic oscillator networks, such as coupled LC circuits, ring oscillators [23, 29], insulator-to-metal transition (IMT) oscillators [7, 24], spin oscillators [25], and integrated complementary metal oxide semiconductor (CMOS) oscillators, have been shown to solve Ising problems. However, there is a lack of theoretical explanation and guidance on designing coupled oscillator networks to generate the desired phase dynamics that efficiently solve Ising problems. If the phase dynamics of the oscillator network follow the Kuramoto model [32], under proper injection locking, its phase dynamics evolve to a ground state that minimizes the Ising cost function [31]. The stability properties of the Kuramoto model’s equilibrium points and the impact of injection signal strength on optimization performance are also analyzed in [33, 34].

In this article, we propose and demonstrate an operational coupled oscillator network based on charge-density-wave (CDW) devices, whose phase dynamics follow the Kuramoto model. The CDW phases are macroscopic quantum states characterized by a periodic modulation of the electronic charge density, accompanied by a small periodic distortion of the atomic lattice [35–38]. The CDW ground state is a condensate of electrons that differ in momentum by $2k_F$, or, in the equivalent interpretation, it is a condensate of $2k_F$ phonons (k_F is the Fermi wave vector). The early models for CDW phases and CDW transport included explicitly quantum mechanical [39] or classical descriptions [40, 41]. Certain phenomena observed in CDW materials, such as quantum creep [42, 43], quantum interference [37], CDW Aharonov-Bohm effect [44], quantum tunneling [45], and CDW quantization [46], require a specific quantum mechanical description. The CDW phases have also been described as ordered quantum fluids that form in layered 1D or 2D van der Waals materials [47, 48]. While some aspects of CDW phenomena can be understood within classical or semi-classical models, one can consider the CDW a fundamentally quantum object. The CDW wavelength is nearly half the de Broglie wavelength of the Fermi-energy electrons, $\lambda = \frac{\pi}{k_f}$. The CDW distortion with this wavelength groups the electrons in pairs, resulting in the energy gap of 2Δ in the electron spectrum at the Fermi level. Owing to the new CDW periodicity superimposed on the crystal lattice, the long phase coherence of the CDW, and the band-gap opening that affects electron transport, a 2D thin film in the CDW phase can be considered a type of quantum well superlattice. In this structure, the modulation of the electron wave function results in the formation of energy gaps.

To illustrate the CDW condensate approach in computing, we experimentally tested the building blocks of the oscillator network – coupled CDW devices with 1T-TaS₂ channels – at room temperature. In the next step, we designed the Ising solver based on a resistively coupled CDW oscillator network, using the relative phase dynamics of each device. Applying second-harmonic injection locking locks the phase of each device into a pair of binary values representing Ising spins. The resistive coupling between each device can represent the connectivity matrix in the Ising cost function.

We demonstrate a CDW oscillator network designed so its phase dynamics follow a behavior similar to the Kuramoto model. To demonstrate the feasibility and efficiency of the proposed CDW oscillator-based Ising solver, we simulate a six-by-six oscillator network to solve Max-Cut benchmark problems. The simulation results show that our oscillators converge to optimal solutions within 10 μs . Thus, using strongly correlated CDW phase transitions instead of conventional resistive switching devices opens the possibility of low-power, scalable information processing for specific types of NP-hard problems.

Two-Dimensional CDW Condensate Materials

Several quasi-one-dimensional (1D) and quasi-two-dimensional (2D) metals reveal the strongly correlated CDW condensate phase [35–38]. These phases unlock new device functionalities via voltage-triggered current non-linearities, the appearance of AC components under DC bias, hysteresis, and other phenomena [38, 49–51]. Interest in CDW condensate phases rapidly intensified after the realization that some phases persist at relatively high temperatures, enabling room-temperature (RT) operation of CDW devices. The 1T polymorph of TaS₂ (1T-TaS₂) is a prominent member of the quasi-2D CDW materials, which reveal three CDW condensate phases the commensurate (C-CDW), nearly commensurate (NC-CDW) and incommensurate CDW phases (IC-CDW)[49, 52, 53]. The CDW phase transitions emerge when changing temperature (see Fig 1a) or electrical bias and are accompanied by hysteresis in the current-voltage (I-V) characteristics (see Fig 1b) [49, 50]. The hysteretic NC-CDW – IC-CDW phase transition, which occurs above RT (see Fig. 1a) and is close to the operation temperatures of modern electronics, makes CDW quantum materials promising candidates as voltage-controlled oscillators (VCOs) [54].

CDW-based quantum oscillators (CDW-QOs) derive functionality from phase transitions where the material’s electronic properties undergo significant changes due to the rearrangement of charge density within the crystal lattice [55]. The associated displacement of the atoms is small. For this reason, CDW devices can function at low power and operate at high speeds [54, 56]. These considerations explain our motivation to search for alternative strongly correlated quantum materials that can provide the functionality required for solving NP-hard problems while simultaneously ensuring potentially low-power dissipation and fast operation. More details comparing other approaches for solving NP-hard problems to CDW-QOs are provided in Section 4.

Experimental and Simulated Results

Electrical Characteristics

The temperature-dependent I-V characteristics of a representative device cooling in steps of 50 K from 360 K to 160 K, with a channel thickness of approximately 15 nm and channel width $\sim 2 \mu\text{m}$, are displayed in Fig. 1b. The hysteresis associated with the NC-CDW – IC-CDW transition exhibits a shape and size consistent with previous reports [49, 57–60]. The I-V curve becomes super-linear before the initial current jump in the hysteresis region due to Joule heating induced by local heating from the current

passage through the channel [54]. The self-heating effect, dependent on the device parameters and voltage sweep rate, induces the NC-CDW – IC-CDW phase transition in these devices [49, 57–60]. Furthermore, inducing CDW phase transitions via an electric field rather than local heating is feasible [50, 57, 61–63]. Fig. 1b illustrates the NC-CDW to IC-CDW phase transition as V_H and the IC-CDW to NC-CDW transition on the reverse bias as V_L . After several months of testing, the fabricated 1T-TaS₂ devices exhibited robustness with reproducible I-V characteristics. Fig. 1a shows the resistance as a function of the temperature measured with a low bias (0.25 mV) for a thicker device ~ 100 nm. These transitions are consistent with prior reports for devices with similar thickness and channel width [49, 58, 64–66].

Charge-Density-Wave Based Quantum Oscillators

The hysteresis exhibited during the phase transition in 1T-TaS₂ enables the generation of voltage-controlled oscillations. This AC characteristic arises from the bistable resistance at a threshold bias voltage along the 1T-TaS₂ channel. Fig. 2a shows the circuit used to make a single CDW-QO device. Fig. 2b shows the intersection of the resistive load line with the I-V hysteresis produced by the device at RT when the DC bias is 4.63 V with $R_S = 2.26$ k Ω . Fig. 2c shows the oscillations produced by the CDW-QO. The experimental results match the simulated results from the analytical expressions discussed in equation (1) and equation (2). Varying V_{DC} while maintaining a constant load resistance ($R_S = 2.26$ k Ω) enables tuning of the oscillation frequency by adjusting the load line–hysteresis intersection as shown in Fig. 2d and described in (3).

Voltage dynamics of the CDW quantum oscillators

We determine the voltage dynamics of a CDW quantum oscillator using device hysteresis, the resistive load line, and the value for parasitic capacitance. Here R_H is the resistance value during the high resistance state, and R_L is the resistance value during the low resistance state. Let R_S denote the circuit’s load resistance and C the parasitic capacitance of the device. Then, the output voltage $V_O(t)$ across the device follows:

$$\begin{cases} \dot{V}_O(t) = -\frac{1}{R_{ch}C}V_O(t) + \frac{1}{R_{ch}C}V_{ch} & (\text{charging}), \\ \dot{V}_O(t) = -\frac{1}{R_{dis}C}V_O(t) + \frac{1}{R_{dis}C}V_{dis} & (\text{discharging}), \end{cases} \quad (1)$$

where $R_{ch} = \frac{R_H R_S}{R_H + R_S}$ and $R_{dis} = \frac{R_L R_S}{R_S + R_L}$ are the equivalent resistances for charging and discharging states, respectively; $V_{ch} = \frac{R_H}{R_H + R_S} V_{DC}$ and $V_{dis} = \frac{R_L}{R_L + R_S} V_{DC}$ are the corresponding equivalent voltages for the charging and discharging states. We denote V_H and V_L as the highest and lowest voltage across a device, respectively. Since the oscillator switches from charging to discharging when $V_O(t) \geq V_H$, and it switches from discharging to charging when $V_O(t) \leq V_L$, the solution of equation (1) is obtained as

$$\begin{cases} V_O(t) = (V_L - V_{ch})e^{-t/(R_{ch}C)} + V_{ch} & (\text{charging}), \\ V_O(t) = (V_H - V_{dis})e^{-t/(R_{dis}C)} + V_{dis} & (\text{discharging}), \end{cases} \quad (2)$$

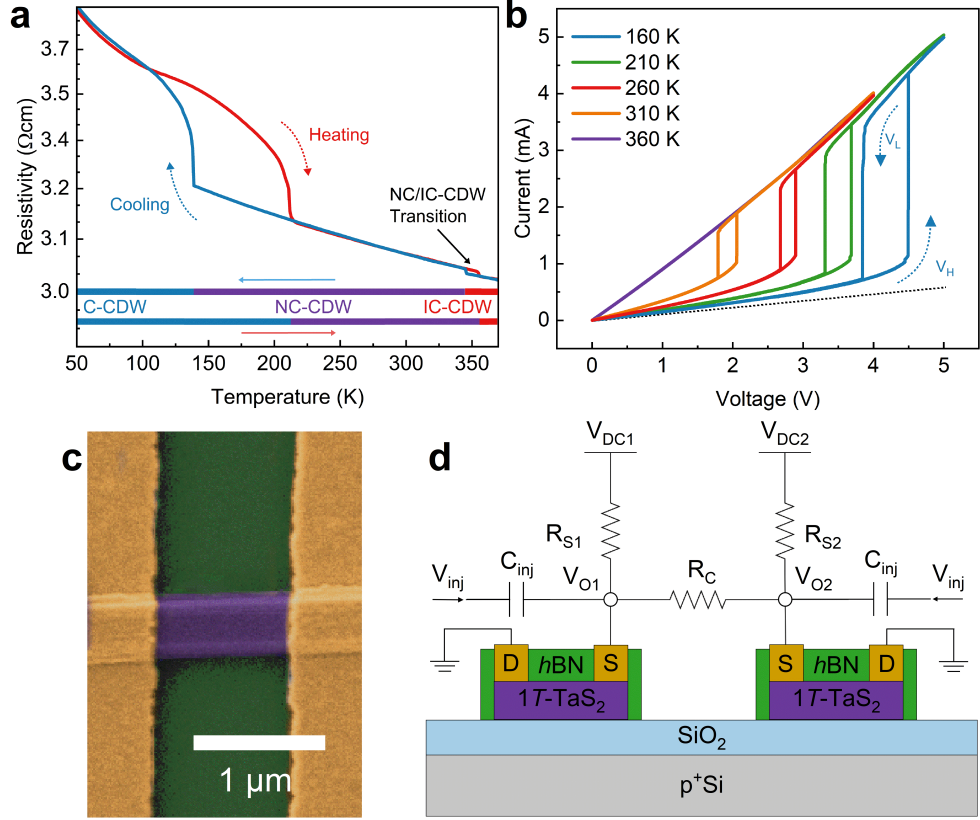


Fig. 1 | Electrical characteristics and circuit configuration of 1T-TaS₂ CDW devices. **a**, Resistivity versus temperature for a CDW device with a ~ 100 -nm-thick channel. **b**, Temperature-dependent I-V characteristics of a 1T-TaS₂ CDW device. **c**, SEM image showing a $\sim 1 \mu\text{m}$ -long 1T-TaS₂ device channel in the coupled oscillator circuit. The pseudo colors are used for clarity. **d**, Circuit schematic of the coupled oscillator device with off-chip coupling resistor R_C , and load resistors R_{S1} . The two devices are powered by an applied DC bias voltage V_{DCi} , and all circuit elements are connected to a common ground. The injection locking signal is applied to both devices through an injection capacitor C_{inj} , and an oscilloscope monitors the output V_{O1} .

and the charging time T_{ch} and discharging time T_{dis} within one oscillation cycle are:

$$\begin{cases} T_{ch} = -\frac{1}{R_{ch}C} \log \frac{V_H - V_{ch}}{V_L - V_{ch}}, \\ T_{dis} = -\frac{1}{R_{dis}C} \log \frac{V_L - V_{dis}}{V_H - V_{dis}}. \end{cases} \quad (3)$$

For the sake of simplicity, in the following context, we use $f(V_O(t))$ to represent the voltage dynamics of a free-running oscillator as in equation (1).

Connecting the outputs of individual oscillators with a resistive component creates a network of oscillators (see Fig. 3a). Pairs of resistively coupled CDW oscillator

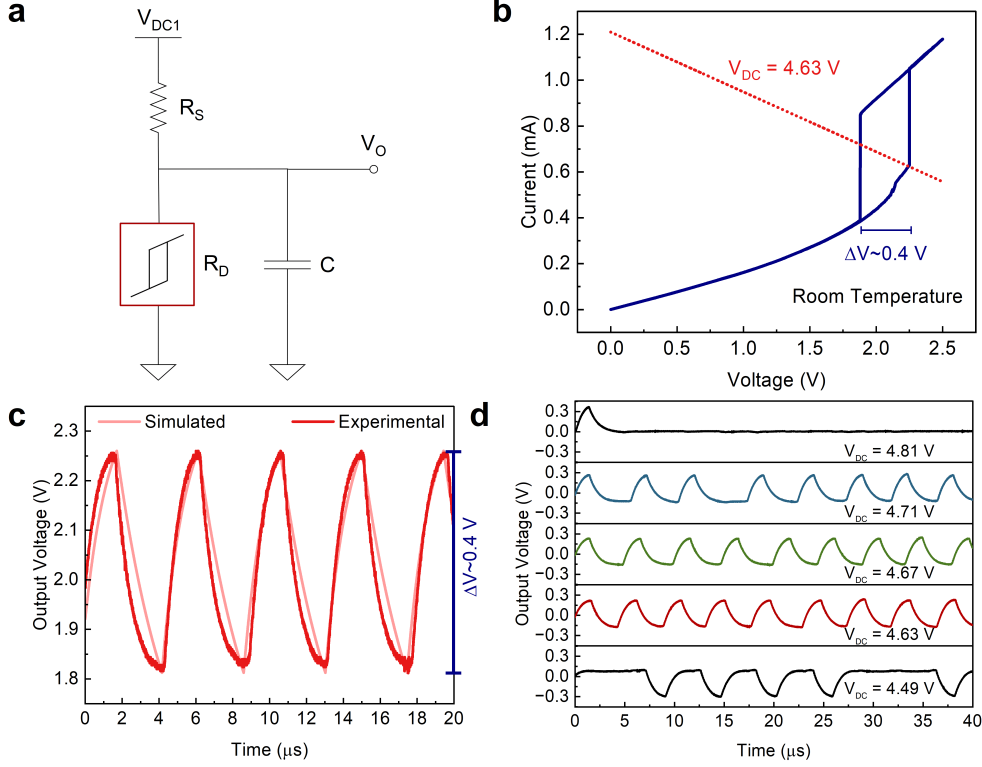


Fig. 2 | Oscillatory Characteristics of a CDW Device at room temperature. **a**, Circuit schematic of a single CDW oscillator device consisting of $1T$ -TaS₂ channel, an off-chip load resistor R_S , and a lumped capacitance C from the output node V_O to ground. An oscilloscope monitors the output terminal. **b**, The hysteresis in the I-V characteristics of a $1T$ -TaS₂ device at room temperature. A resistive load line from the circuit described in **a** intersects the hysteresis. The width of the hysteresis is $\Delta V \sim 0.4$ V. **c**, Oscillations produced by the circuit shown in **a**. These oscillations only occur when the voltage across the device intersects the hysteresis, as shown in **b**. Pink traces represent simulated oscillations, and red traces indicate experimental results obtained at room temperature. **d**, The frequency of stable oscillations changes as the applied DC bias is adjusted. At $V_{DC} = 4.49$ V, the oscillations begin. Increasing to $V_{DC} = 4.63$ V, 4.67 V, and 4.71 V, oscillations stabilize with $f = 219$ kHz, 208 kHz, and 195 kHz. At $V_{DC} = 4.81$ V, the oscillations become unstable. The output voltage is normalized.

devices are investigated experimentally with numerical studies and analytical simulation. Coupling two devices with the correct coupling resistor, R_C , allows the oscillator frequency to lock when the natural frequency of the oscillators is comparable. Fig. 3a shows the circuit used to couple two CDW oscillator devices. The input voltages V_{DC1} and V_{DC2} , as well as the load resistances R_{S1} and R_{S2} are selected to ensure stable oscillation states for the individual CDW-QOs. We tune the load resistors R_{S_i} individually for each $1T$ -TaS₂ device, using the average resistance between the IC-CDW and NC-CDW resistive states. Adjusting V_{DC_i} , R_{S_i} , and R_C allows for various phase relationships between the oscillators. Before coupling, CDW-QOs oscillate at

their natural frequencies, as shown in the lower panel of Fig. 3d. The intersection of the load line with the hysteresis of the device determines the oscillation dynamics. The coupling resistance R_C is determined based on the desired coupling strength. A higher coupling resistance yields weaker coupling; a lower resistance yields stronger coupling. Strong coupling aligns the oscillators in phase, while weak coupling shifts them out of phase. Fig. 3d demonstrates this concept. The bottom panel shows oscillators before coupling where the oscillators are oscillating at their natural frequencies $f_1 = 537$ kHz (red) and $f_2 = 476$ kHz (blue).

We assume that the differences between the oscillators can be neglected, namely $f(V_{O_i}(t)) \approx f(V_{O_j}(t))$, $\forall i, j \in \{1, 2, \dots, N\}$. When the i th oscillator is coupled with other oscillators through the coupling resistance R_{ij} , with $j = \{1, 2, \dots, N\}$, its voltage follows

$$\dot{V}_{O_i}(t) = f(V_{O_i}(t)) - \underbrace{\sum_{j=1}^N \frac{1}{R_{ij}C} (V_{O_i}(t) - V_{O_j}(t))}_{\text{coupling term}}, \quad (4)$$

where coupling is driven by the currents $I_{ij}(t) = \frac{1}{R_{ij}}(V_{O_i}(t) - V_{O_j}(t))$ flowing from the i -th oscillator to other oscillators connected through the coupling resistance R_{ij} . We assume the oscillator network is weakly coupled, meaning that the R_{ij} are chosen to be sufficiently large such that the currents $I_{ij}(t)$ are small. Let $\theta_i(t)$ denote the phase of the i -th oscillator. When the oscillator is free running, we have $\dot{\theta}_i(t) = \omega_0$, where $\omega_0 = 2\pi/(T_{\text{ch}} + T_{\text{dis}})$ is the natural angular frequency. Using phase reduction theory [67], we show that the phase dynamics of the coupled oscillator network in equation (4) can be approximated by

$$\dot{\theta}_i(t) \approx \omega_0 - \sum_{j=1}^N J_{ij} \sin(\theta_i(t) - \theta_j(t)), \quad (5)$$

where $J_{ij} = A/(R_{ij}C)$ and A is a constant. We provide the derivation of the phase dynamics of the coupled CDW oscillator network in ‘‘Methods’’. We neglect differences between oscillators, assign each oscillator the same natural frequency ω_0 , and use $\phi_i(t) = \theta_i(t) - \omega_0 t$ as the relative phase for each oscillator.

Solving combinatorial optimization problems using CDW-QO networks

Physicists first studied the Ising model in the 1920s as a mathematical framework to explain domain formation in ferromagnets [1, 2]. The model comprises N variables $\mathbf{x} = [x_1 \ x_2 \ \dots \ x_N]$, where each variable x_i represents a spin that takes values in $\{+1, -1\}$

and minimizes an “energy function,” known as the Ising Hamiltonian function:

$$H(\mathbf{x}) = - \sum_{1 < i < j < N} W_{ij} x_i x_j, \text{ with } x_i, x_j \in \{-1, +1\}, \quad (6)$$

where W_{ij} are real coefficients. The Ising model’s appeal stems from its ability to map real-world optimization problems directly to determine the ground-state solution of equation (6) [68]. However, such problems belong to the NP-hard or NP-complete complexity classes. Computing their solutions with digital computers requires exponentially growing resources as the problem size increases, making it difficult to solve problems of moderate size efficiently.

To represent the Ising spins $x_i, x_j \in \{-1, +1\}$ defined in the Ising Hamiltonian cost function using $\{\phi_i(t)\}$, we need to lock $\{\phi_i(t)\}$ to a pair of binary values. Previous work [69–71] demonstrates that by injecting an external periodic signal with an appropriate magnitude to each device, $\{\phi_i(t)\}$ can be locked to a certain phase configuration. To do so, the frequency of the injected signal should be an integer multiple of the device’s natural frequency. In our settings, we choose a sinusoidal injection signal, $V_{\text{inj}}(t) = A_{\text{inj}} \sin(n\omega_0 t)$, where A_{inj} is the magnitude of the injected signal and n is a positive integer.

The schematic circuit of a single CDW-QO is shown in Fig. 3b, where an injection signal V_{inj} is applied to the output V_{O1} through the injection capacitor C_{inj} . The circuit describing the pair of coupled CDW oscillators with injection locking is shown in Fig. 3c. As shown in [69–71], the case of first-harmonic injection locking (FHIL) emerges when the frequency of $V_{\text{inj}}(t)$ equals ω_0 , i.e., $V_{\text{inj}}(t) = A_{\text{inj}} \sin(\omega_0 t)$, $\{\phi_i(t)\}$ can be locked to the phase of the injection signal in the steady state. When the frequency of $V_{\text{inj}}(t)$ is twice the natural frequency ω_0 , i.e., $V_{\text{inj}}(t) = A_{\text{inj}} \sin(2\omega_0 t)$, $\{\phi_i(t)\}$ can be locked to a pair of binary values in the steady state. This corresponds to the case of second harmonic injection locking (SHIL). Fig. 3e shows the experimental response of a CDW-QO to an injection signal. Here, the bottom panel shows the free-running oscillator, the middle panel shows the response of the CDW-QO to FHIL, and the top panel shows the response of the oscillator to SHIL. The free-running oscillator has an infinite number of stable phase configurations; under FHIL, the CDW-QO has only one stable phase configuration, and with SHIL, there are two stable phase configurations. It should be noted that, for the case of the free running and the SHIL, only one stable phase configuration is shown in Fig. 3e.

For the case of coupled CDW-QOs, Fig. 3c shows the circuit describing injection locking the network. Fig. 3f demonstrates the three injection locking scenarios of a pair of coupled CDW-QOs experimentally. The bottom panel shows a pair of strongly coupled oscillators ($R_C = 3 \text{ k}\Omega$) before injection locking. The middle panel shows the coupled oscillators under FHIL, where the phase of both oscillators synchronize with the injection signal. The top panel shows one of the bistable configurations of the CDW-QOs under SHIL.

Three different injection-locking scenarios are experimentally demonstrated in the context of two weakly coupled oscillators in Fig. 4. Similar to the central panel of Fig. 3d, Fig. 4a shows the oscillations formed from weak coupling without injection locking. Fig. 4b shows the FHIL of a coupled pair of CDW-QOs, where we linearly anneal

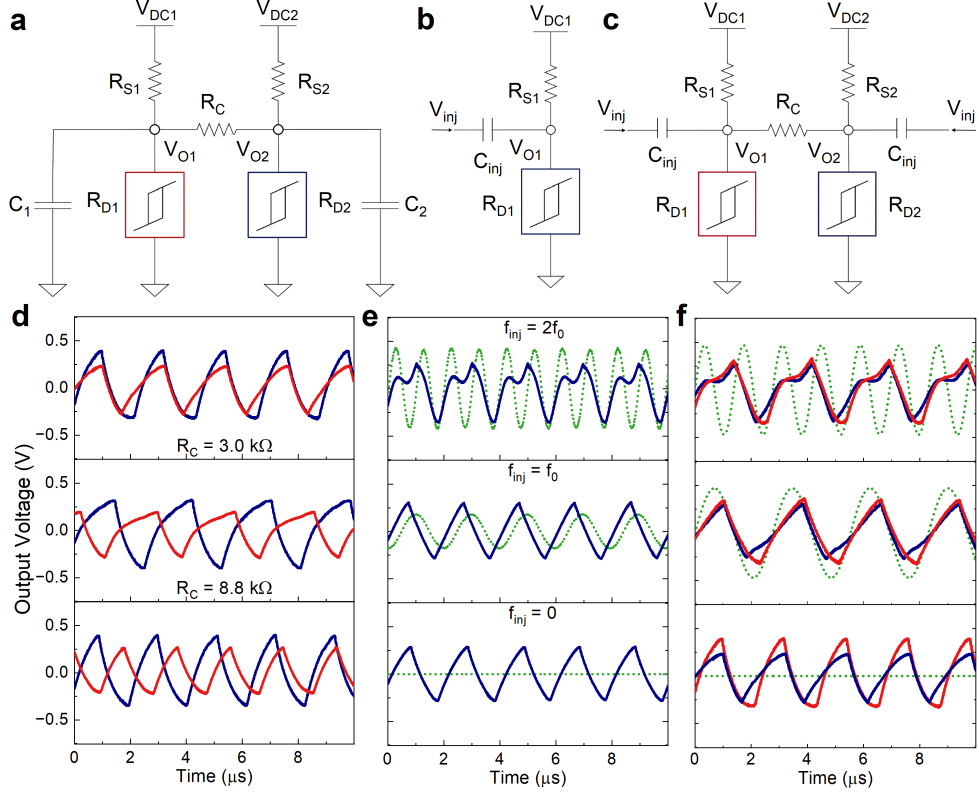


Fig. 3 | Oscillatory dynamics of coupled and injection-locked CDW-QOs. **a**, Circuit describing two resistively coupled CDW oscillator devices. **b**, Circuit describing the injection locking of a single CDW-QO. **c**, The injection locking signal is applied to two resistively coupled CDW-QOs. **d**, Coupling scenarios for a pair of coupled CDW-QOs described by the circuit in **a**. Adjusting the coupling resistance tunes the phase of the frequency-locked coupled oscillators. A larger coupling resistance results in a smaller coupling between oscillators. **e** Injection locking scenarios for a single oscillator described by the circuit in **b**. The green dotted line represents the injection signal. Three scenarios are depicted (bottom to top): before injection locking, FHIL, and SHIL after annealing to the stable solution. **f** Injection locking scenarios of coupled CDW-QOs as described by the circuit in **c**. Three scenarios are depicted (bottom to top): Strong coupling before injection locking, after FHIL, and after SHIL. Note the output voltage is normalized for **d**, **e**, and **f**.

the injection amplitude to $A_{inj} = 2$ V. For the case of SHIL, each oscillator exhibits bistability, meaning they will settle into one of the two phase-locked states, effectively binarizing the phase. Fig. 4c shows one of the two stable phases of the oscillators where the oscillators are in phase with one another. Fig. 4d shows the other stable phase where the CDW-QOs are out of phase with one another. The experimental results for these three scenarios have been confirmed with numerical simulations, as shown in light blue and light red in Fig. 4.

We also simulate the scenarios of FHIL and SHIL for a pair of homogeneous coupled CDW-QOs. For FHIL, the voltage waveforms of the two oscillators are in-phase and

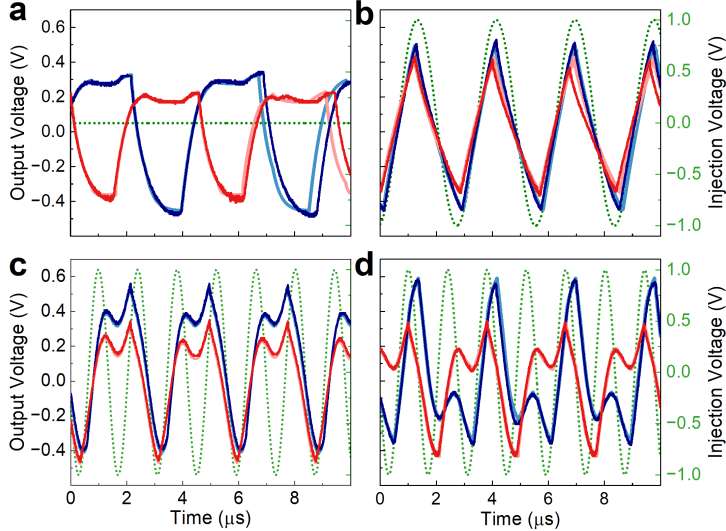


Fig. 4 Experimental injection-locking scenarios. **a**, In the absence of injection locking, weakly coupled oscillators synchronize in frequency but not in phase, resulting in a flat energy landscape for the phase space. **b**, With FHIL, the oscillators synchronize their phases with the injection locking signal. **c,d**, For SHIL, the oscillator phase is in a bi-stable state and has in-phase **c**, and out-of-phase **d**, configurations to the input with equal probability. The green dotted line shows the injection locking signal. Simulated results, shown in light blue and light red, demonstrate the oscillators fit the theoretical framework.

locked to the input signal (see Fig. 5b). Then we simulate their phase dynamics $\phi_1(t)$ and $\phi_2(t)$ using equation (17) for 10 experiments with randomly generated initial values between 0° and 360° . We notice that $\phi_1(t)$ and $\phi_2(t)$, starting from different initial values, are all locked to 117° in the steady state, as shown in Fig. 5e. For SHIL, the voltage waveforms of the two oscillators exhibit in-phase and out-of-phase configuration with respect to the input signal, as shown in Fig. 5c. We also simulated their phase dynamics $\phi_1(t)$ and $\phi_2(t)$ following equation (17) for 20 experiments with randomly generated initial values. We observe that $\phi_1(t)$ and $\phi_2(t)$ starting from different initial values converge to a pair of binarized phase values: 112° and 292° (see Fig. 5f). For the case of zero injection signal, we simulate the phase evolution of $\phi_1(t)$ and $\phi_2(t)$ for 10 experiments with randomly generated initial values. As shown in Fig. 5f, they settle to many different values spread out in the phase domain.

Under SHIL, the oscillator phase responses $\{\phi_i(t)\}$ are locked to a pair of binary phase values $\{112^\circ, 292^\circ\}$ differing by 180° , which we use to represent the Ising spins $\{-1, +1\}$ in equation (6). This phenomenon is demonstrated in various types of oscillators [31, 70]. The bi-stability of $\phi(t)$ offers a method for encoding the Ising spin within the electrical domain, and mapping the bi-stable behavior to the Ising spins allows for solving combinatorial optimization problems such as the Max-Cut. The simulated results demonstrate the oscillators fit the theoretical framework and thus can

be used to scale up the problem. A comprehensive analysis of the coupled CDW oscillator network’s phase dynamics $\{\phi_i\}$ is provided in “Method,” which also discusses how SHIL can be used to lock $\{\phi_i\}$ to a pair of values that can represent Ising spins.

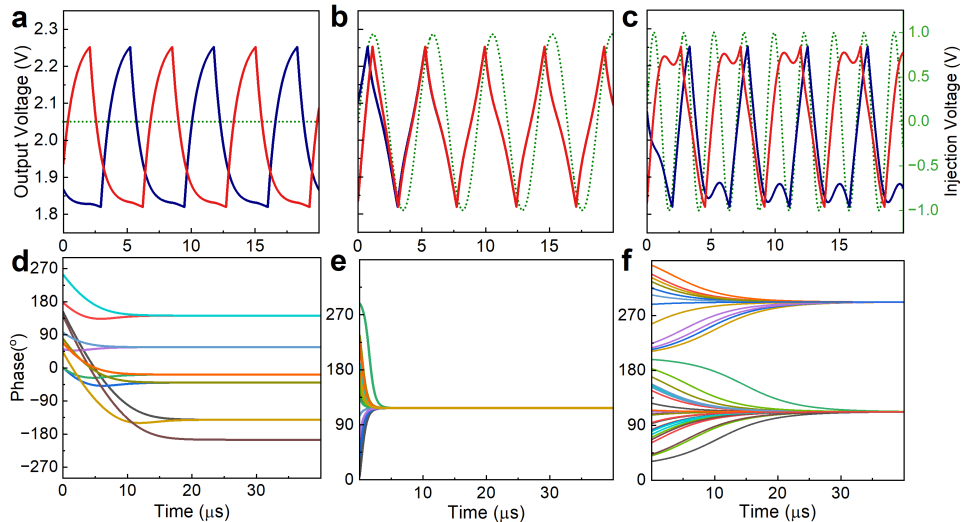


Fig. 5 Phase evolution of three distinct injection-locking scenarios. **a,d**, In the absence of synchronization, the free-running oscillators exhibit uniform phases across the phase space. **b,e**, For FHIL, the oscillators are in-phase and locked with the injection signal. Their corresponding phases $\phi_1(t)$ and $\phi_2(t)$ with different random initial values converge to the locked phase value 117° . **c,f**, For SHIL, the oscillators exhibit in-phase and out-of-phase steady-state waveforms locked to the injection signal, and $\phi_1(t)$ and $\phi_2(t)$ with random initial values converge to the bi-stable phase values 112° and 292° with 50% probability respectively.

Benchmark examples in solving the Max-Cut problem

We demonstrate our CDW oscillator network’s feasibility and efficacy by solving a class of Ising Hamiltonian problems: The maximum cut problem (Max-Cut). Max-Cut is one of the most straightforward graph partitioning problems to conceptualize, yet one of the most challenging combinatorial optimization problems to solve [72]. Its objective is to partition the set of vertices of a graph into two subsets, such that the sum of the weights of the edges having one endpoint in each of the subsets is maximized. The proper definitions of a graph and a cut are given as follows:

Definition 1. Let $\mathcal{G} = (V, E)$ be an un-directed graph, where V is the vertex set and E is the edge set. Let $W := \{W_{ij}\}$ be the weights of each edge in the graph. A cut is defined as a partition of the vertex set into two disjoint subsets S and $V \setminus S$. The weight of the cut $(S, V \setminus S)$ is given by

$$C(S) := \sum_{i \in S, j \in V \setminus S} W_{ij}. \quad (7)$$

Definition 2. The maximum cut of the graph $\mathcal{G} = (V, E)$ with weight W is defined as

$$C^*(S) := \max_{\forall S \subseteq V} C(S). \quad (8)$$

The MAX-CUT problem seeks to find a subset of vertices such that the total weights of the cut set between this subset and the remaining vertices are maximized. Let $x_i = 1$ if $i \in S$ or $x_i = -1$ if $i \in V \setminus S$, then $C(S)$ can be written as

$$C(S) = \frac{1}{2} \sum_{1 \leq i < j \leq n} W_{ij}(1 - x_i x_j) = \frac{1}{2} \sum_{1 \leq i < j \leq n} W_{ij} - W_{i,j} x_i x_j. \quad (9)$$

Let $\mathbf{x} = [x_1 \ x_2 \ \dots \ x_N]$ and define $H(\mathbf{x}) = \sum_{1 \leq i < j \leq n} W_{ij} x_i x_j$. If we choose $J_{ij} = -W_{ij}$, $H(\mathbf{x})$ is in the form of the Hamiltonian cost function in equation (6). Therefore, maximizing the cut values $C(S)$ is equivalent to minimizing the Hamiltonian cost function $H(\mathbf{x})$ with respect to $J_{ij} = -W_{ij}$.

To investigate the performance of the CDW coupled oscillator network as Ising Hamiltonian solvers, in our simulation setup, we choose an undirected and unweighted graph with 6 nodes as shown in Fig. 6a, with connectivity (adjacency) matrix

$$W = \frac{1}{CR_C} \begin{pmatrix} 0 & 1 & 1 & 1 & 0 & 0 \\ 1 & 0 & 1 & 1 & 1 & 1 \\ 1 & 1 & 0 & 1 & 0 & 1 \\ 1 & 1 & 1 & 0 & 1 & 1 \\ 0 & 1 & 0 & 1 & 0 & 0 \\ 0 & 1 & 1 & 1 & 0 & 0 \end{pmatrix}. \quad (10)$$

There are two sets of optimal partitions to obtain the maximum cut value $C^*(S) = \frac{8}{CR_C}$:

$$x_2 = x_3 = x_4 = 1, \ x_1 = x_5 = x_6 = -1, \quad (11)$$

and

$$x_2 = x_4 = 1, \ x_1 = x_3 = x_5 = x_6 = -1. \quad (12)$$

Fig 6b depicts the circuit illustration of our six-by-six coupled CDW oscillator network. Each oscillator connected to others through coupling resistances of equal magnitude $R_C = 43.727 \text{ k}\Omega$, following the connectivity matrix W in equation (10). The same SHIL signal is applied to each oscillator through the injection capacitance C_{inj} .

Fig. 6d and Fig. 6e show our simulation results. We first randomly initialize the voltage values $\mathbf{v}_i(t)$ for each oscillator. As shown in Fig. 6c, we observe that $\mathbf{v}_2(t)$, $\mathbf{v}_3(t)$ and, $\mathbf{v}_4(t)$ are anti-phase synchronized with $\mathbf{v}_1(t)$, $\mathbf{v}_5(t)$ and $\mathbf{v}_6(t)$ after $t \approx 10 \mu\text{s}$. We also observe that their corresponding phases $\phi_2(t)$, $\phi_3(t)$ and $\phi_4(t)$ converge to 298° , which is 180° different from the phase value 115° that $\phi_1(t)$, $\phi_5(t)$ and $\phi_6(t)$ converge to, as shown in Fig. 6e. Thus, the simulation results demonstrate that the

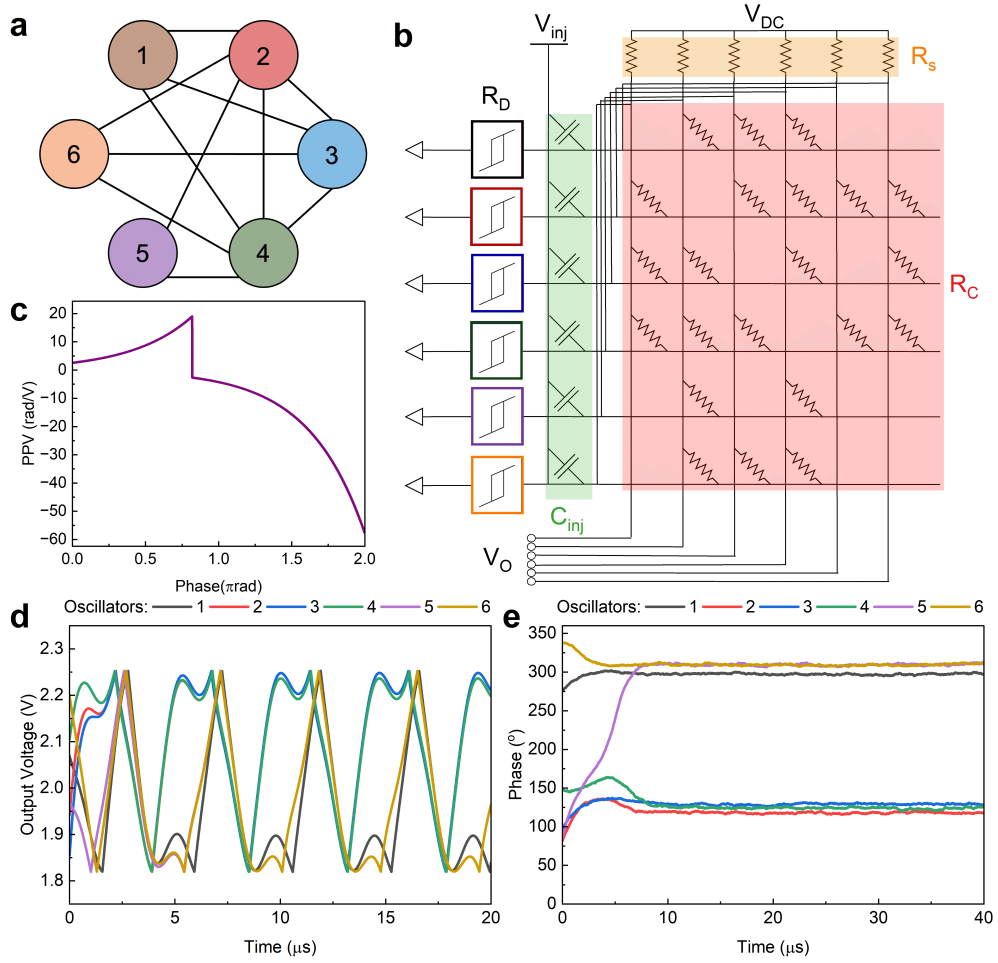


Fig. 6 The simulated results from solving Max-Cut optimization problems. **a**, The 6×6 connected graph, where the weight of all the edges equals $1/(CR_C)$. **b**, Circuit representation of the 6 coupled oscillators using the weights described in the connectivity matrix. **c**, The values of the phase sensitivity function over 0 to 2π . **d**, The voltage waveforms of oscillators 1, 5, and 6 are synchronized, while oscillators 2 and 3 are synchronized with oscillator 4. **e**, The phase evolution of the six-dimensional oscillator network. In the steady state ϕ_1 , ϕ_5 and ϕ_6 converge to 115° , whereas ϕ_2 , ϕ_3 , and ϕ_4 converge to 298° .

steady states of the six coupled oscillators give one optimal partition that solves the Max-Cut problem for the graph in equation (11).

Methods

Fabrication

Bulk 1T-TaS₂ crystals were grown using the chemical vapor transport method (CVT)[73]. Thin layers of 1T-TaS₂ were prepared by mechanical exfoliation and placed onto a SiO₂/p⁺Si substrate using an in-house transfer system. The ability to fabricate CDW-QOs on SiO₂ substrates highlights their seamless compatibility and potential for integration with existing Si CMOS technology. A thin *h*-BN capping layer was applied atop the 1T-TaS₂ layers to protect samples during nanofabrication and prevent environmental damage. Electron-beam lithography (EBL) was employed to fabricate two-terminal device structures. Atomic layer etching of the *h*-BN with SF₆ plasma exposes the 1T-TaS₂ flake, enabling deposition of Ti/Au (10 nm/100 nm) metal contacts via Electron Beam Evaporation (EBE). Fig. 1c shows a false color SEM image of a two-terminal device with a channel width of $\sim 1 \mu\text{m}$. Fig. 1d shows a schematic of a pair of devices used in this study. The schematic illustrates a pair of coupled 1T-TaS₂ devices on a Si/SiO₂ substrate, covered with *h*-BN, accompanied by off-chip load resistors R_{si} , coupling resistance R_C , parasitic capacitance C_i , injection signal V_{inj} , and injection capacitance C_{inj} . Both devices are energized by a DC bias voltage V_{DC} , with all circuit components connected to a shared ground. An oscilloscope reads the output voltage V_{O_i} , and we measure the phase of the oscillators under various coupling configurations.

Electrical Measurements

Temperature-dependent electrical characterization of the 1T-TaS₂ devices was performed using a cryogenic probe station (Lakeshore TTPX) and a semiconductor parameter analyzer (Agilent B1500A). A cryogenic temperature controller (Lakeshore 336) maintained the environmental temperature. Heating and cooling rates were set at a constant 2 K/min using the Lakeshore Measure LINK software to ensure accurate temperature readings and preserve sample integrity. For the current-voltage (I-V) measurements, the applied bias voltage was swept across the device channel at a rate of 200 mV/s with a step size of 2 mV. We use a Teledyne LeCroy WaveAce 1012 oscilloscope to capture the waveform's oscillating signal, while a BK Precision 1787B provides a constant DC voltage bias to the circuit. The Teledyne Lecroy Wavestation 2012 waveform generator provides the injection locking signal to the oscillator circuit for both FHIL and SHIL scenarios.

Phase dynamics of the coupled oscillators

When an oscillator connects with other oscillators in the network through the coupling resistance R_{ij} , we have

$$\dot{\theta}_i(t) = \omega_0 - \sum_{j=1}^N \frac{1}{R_{ij}C} \Gamma(\theta_i(t) - \theta_j(t)), \quad (13)$$

where

$$\Gamma(\theta_i(t) - \theta_j(t)) = \frac{1}{2\pi} \int_0^{2\pi} Z(\theta_i(t) - \theta_j(t) + \psi)(V_O(\theta_i(t) - \theta_j(t) + \psi) - V_O(\psi))d\psi \quad (14)$$

is the phase coupling function and $Z(\theta) = \frac{\partial\theta(t)}{\partial V_O}$ is the 2π periodic phase sensitivity function [67]. One straightforward method to compute $Z(\theta)$ numerically is to use its definition: $Z(\theta) = \lim_{\Delta V_O \rightarrow 0} \frac{\Delta\theta}{\Delta V_O}$. Specifically, we perturb the limit cycle voltage dynamics $f(V_O(t))$ by adding $\Delta V_O = 0.01$ over 1170 steps covering one charging and discharging cycle. We compare the perturbed waveform $\tilde{V}_O(t)$ to the original waveform V_O , and measure the time shift ΔT between their switching points. Then, the corresponding phase shift is calculated as $\Delta\theta = 2\pi\Delta T/(T_{\text{ch}} + T_{\text{dis}})$. Fig. 6c shows the calculated phase sensitivity function waveform over the interval of 0 and 2π .

Following equation (14), we numerically calculate the phase coupling function $\Gamma(\theta_i(t) - \theta_j(t))$ over 0 to 2π and we further observe that $\Gamma(\theta_i(t) - \theta_j(t))$ can be approximated by a sinusoidal function as $A \sin(\theta_i(t) - \theta_j(t) + \alpha) + \beta$, with $A = -1.93$, $\alpha = 0.06439$ and $\beta = -0.1033$, see Fig. S4b. This indicates that the phase response of the CDW-coupled oscillators follows dynamics similar to Kuramoto oscillators [74]. Since the values of α and β are determined by the oscillator's voltage dynamics, it is possible to adjust the device temperature and circuit variables, such as the DC voltage and load resistance values, to generate the desired phase coupling functions. Other examples [75, 76] also show that many oscillators, such as LC and ring oscillators, have the flexibility to tune the dynamics to yield the desired phase coupling functions.

Assuming the differences between oscillators can be neglected and every oscillator has the same natural frequency ω_0 , we introduce the relative phase: $\phi_i(t) = \theta_i(t) - \omega_0 t$ for each oscillator, where $\phi_i(t)$ obeys

$$\dot{\phi}_i(t) = \dot{\theta}_i(t) - \omega_0 = - \sum_{j=1}^N \frac{1}{R_{ij}C} \Gamma(\phi_i(t) - \phi_j(t)). \quad (15)$$

Fig. 3c shows the schematic circuit of coupled oscillators with the injection signal. Since $V_{\text{inj}}(t)$ is applied through a capacitor C_{inj} , the corresponding injected current is $I_{\text{inj}}(t) = C_{\text{inj}} \frac{dV_{\text{inj}}(t)}{dt} = C_{\text{inj}} n\omega_0 A_{\text{inj}} \cos(n\omega_0 t)$. Then, the coupled voltage dynamics in equation (4) with the injection signal can be modified as

$$\dot{\mathbf{v}}_i(t) = f(\mathbf{v}_i(t)) - \sum_{j=1}^N \frac{1}{R_{ij}C} (\mathbf{v}_i(t) - \mathbf{v}_j(t)) + \frac{1}{C} I_{\text{inj}}(t), \quad (16)$$

and the phase dynamics of the CDW oscillator network with injection signals becomes

$$\dot{\phi}_i(t) = - \sum_{j=1}^N \frac{1}{R_{ij}C} \Gamma(\phi_i(t) - \phi_j(t)) + \underbrace{K_s \int_0^{2\pi} Z(\phi_i(t) + \psi) \cos(n\psi) d\psi}_{\text{injection term}}, \quad (17)$$

where $K_s = 1/2\pi C_{\text{inj}}/Cn\omega_0 A_{\text{inj}}$. To explore how to use the binary phase values to represent the spin assignments of the cost function in equation (6), next, we analyze the dynamics of $\{\phi_i(t)\}$ under SHIL. First, we numerically calculate the injection term in equation (17) for $n = 2$, i.e., the SHIL scenario for $\phi_i(t)$ over the interval of 0 to 2π (see Supplemental Fig. S5c, solid line). The injection term can be approximated using a sinusoidal function: $A_1 \cos(2\phi_i(t) + \alpha_1) + \beta_1$, with $A_1 = 4.05$, $\alpha_1 = -2.31$ and $\beta_1 = 0.0014$ (see Supplemental Fig. S5c, dashed line). Since the phase coupling function $\Gamma(\phi_i(t) - \phi_j(t))$ can be approximated by $A \sin(\phi_i(t) - \phi_j(t) + \alpha) + \beta$, where α and β are small, and the injection term in equation (17) can be approximated by $A_1 \cos(2\phi_i(t) + \alpha_1) + \beta_1$, where β_1 is also small, the dynamics of $\phi_i(t)$ in equation (17) can be approximated as:

$$\dot{\phi}_i(t) \approx - \sum_{j=1}^N J_{ij} \sin(\phi_i(t) - \phi_j(t)) + K_s \cos(2\phi_i(t) + \alpha_1), \quad (18)$$

where $J_{ij} = A/(R_{ij}C)$ and $K = A_1 K_s$. Let $\tilde{\alpha}_1 = \alpha_1/2 - \pi/4$, then $\dot{\phi}_i(t)$ can be rewritten as

$$\dot{\phi}_i(t) = - \sum_{j=1}^N J_{ij} \sin(\phi_i(t) - \phi_j(t)) - K_s \sin(2\phi_i(t) + 2\tilde{\alpha}_1), \quad (19)$$

which is the gradient flow of the following function

$$- \sum_{1 \leq i < j \leq N} J_{ij} \cos(\phi_i(t) - \phi_j(t)) + K_s \sin^2(\phi_i(t) + \tilde{\alpha}_1). \quad (20)$$

We observe that equation (20) is the relaxed version, with penalty coefficient K_s , of the following optimization problem :

$$\begin{aligned} \min_{\phi_1, \dots, \phi_N} \quad & - \sum_{1 \leq i < j \leq n} J_{ij} \cos(\phi_i(t) - \phi_j(t)) \\ \text{subject to} \quad & \sin(\phi_i(t) + \tilde{\alpha}_1) = 0, \text{ for } i \in \{1, \dots, N\}. \end{aligned} \quad (21)$$

The optimization problem given by equation (21) is equivalent to the Ising problem in equation (6) because the constraint limits $\phi_i + \tilde{\alpha}_1$ to be either 0 or π , which leads to $\cos(\phi_i(t) - \phi_j(t)) \in \{1, -1\}$ for $i, j \in \{1, \dots, N\}$.

By carefully tuning the penalty coefficient K_s of the constraint term in equation (21), we can lock $\phi_i(t)$ at the binary phase values $\{112^\circ, 292^\circ\}$ that correspond to $\sin(\phi_i(t) + \tilde{\alpha}_1) = 0$ and $\cos(\phi_i(t) - \phi_j(t)) \in \{1, -1\}$, as observed in our simulation of two coupled oscillators under SHIL. However, some equilibrium points might exist ($\dot{\phi}(t) = 0$) that correspond to local minima of equation (21) that do not yield the optimal solution to the Ising Hamiltonian problem, as discussed in [33, 34]. A comprehensive analysis of equilibrium points and their structural and stability properties is carried out in [34]. For more details, we refer readers to this source.

Other experimental works [69, 77] for VO₂ oscillators demonstrate that the local minima are numerically avoided by slowly increasing the injection strength (annealing). Applying annealing improves the success rates of VO₂ oscillators in solving combinatorial optimization problems. One interesting future direction for our setups would be analyzing the energy landscape of the CDW oscillator’s phase dynamics to provide theoretical design methods and guarantees to reduce the effects of local minima.

Additional Benefits of CDW Oscillator Devices

CDW oscillators with 1*T*-TaS₂ channels can be implemented on SiO₂ / Si substrates, simplifying their integration with conventional Si CMOS technology. The demonstrated IMT devices, e.g. with VO₂ active layers, have utilized TiO₂ [7], and conductive TiN [78] substrates or were deposited on SiO₂ using pulsed laser deposition (PLD) and atomic layer deposition (ALD) [79]. The maximum frequency of oscillations reported for a VO₂ device on SiO₂ is 100 kHz [79]. Furthermore, limitations in the frequency of oscillations achievable by VO₂, as indicated by electrothermal simulations [80], restrict its utility in applications requiring higher frequencies and hinder the necessary time to reach a stable solution. In this study, individual 1*T*-TaS₂ devices have exhibited stable oscillations up to 3.3 MHz at room temperature with an amplitude of just 0.01 V, showcasing the versatility of 1*T*-TaS₂ CDW-QOs across a broad frequency spectrum with low power output (see Fig. S4). Oscillatory neural networks (ONNs) encode information by maintaining a stable phase difference between each oscillator in the network and a reference oscillator, achieved during synchronization [81, 82]. The computational energy consumed by ONNs is directly proportional to their settling time [83], which is determined by the number of cycles required for synchronization multiplied by the oscillation period. Increasing the oscillator frequency and amplitude of oscillations will reduce the overall energy consumption of CDW-QO operations.

Radiation-induced damage is a significant challenge in modern electronics [84], particularly in the harsh environment of outer space [85]. The performance of CMOS devices can significantly deteriorate under X-ray or proton irradiation [86]. Total ionizing dose (TID) irradiation can create electron-hole pairs within the oxide layers and at the interfaces in field-effect transistor (FET) structures [87, 88]. The accumulation of charge carriers can significantly affect the electrical characteristics and overall performance of the CMOS device. This degradation underscores the need to develop radiation-hardened electronics that overcome CMOS technology’s physical limits by engineering circuits from radiation-resistant materials. VCOs operating at RT built using CDW phase transitions in quasi-2D 1*T*-TaS₂ are a strong alternative [54]. CDW materials, being metals with high electron concentrations, are inherently more radiation-resistant than semiconductors. The radiation hardness of 1*T*-TaS₂ VCOs against X-rays has been experimentally confirmed [87].

Another aspect to consider is the difference between CDW phase transitions in 1*T*-TaS₂ and IMT phase transitions in materials such as VO₂ [89]. VO₂ undergoes a reversible polymorph phase transition from a semiconducting monoclinic phase to a metallic rutile phase at ~ 340 K. 1*T*-TaS₂ experiences a reversible CDW phase transition from the more resistive NC-CDW state to the less resistive IC-CDW state.

In CDW phase transitions, the material’s electronic properties undergo significant changes due to the rearrangement of charge density within the crystal lattice. The transition in $1T$ -TaS₂ does not involve a polymorph change but rather a resistance transition due to the switching between CDW states.

Conclusions

We demonstrated an approach for solving certain NP-hard problems using coupled oscillator networks implemented with CDW quantum condensate devices. We built and tested prototype hardware based on the $1T$ polymorph of TaS₂, which revealed the switching between the CDW electron-phonon condensate phases above room temperature. The oscillator operation relies on hysteresis in the I-V characteristics and bistability triggered by applied electrical bias. The designed injection-locked, coupled oscillator network reveals the phase dynamics that follow the Kuromoto model. We demonstrate that the phase dynamics of such coupled quantum oscillators evolve to the ground state, which solves combinatorial optimization problems. The coupled oscillators based on charge-density-wave condensate phases can efficiently solve NP-hard Max-Cut benchmark problems, offering advantages over other leading oscillator-based approaches. The quantum nature of the transitions between the CDW phases, distinctively different from resistive switching, creates the potential for low-power operation and compatibility with conventional Si technology.

References

- [1] E. Ising, Beitrag zur theorie des ferro-und paramagnetismus. Ph.D. thesis, Grefe & Tiedemann Hamburg, Germany (1924)
- [2] W. Lenz, Beitrag zum verständnis der magnetischen erscheinungen in festen körpern. Z. Phys. **21**, 613–615 (1920)
- [3] C.D. Schuman, S.R. Kulkarni, M. Parsa, J.P. Mitchell, B. Kay, et al., Opportunities for neuromorphic computing algorithms and applications. Nature Computational Science **2**(1), 10–19 (2022)
- [4] F. Cai, S. Kumar, T. Van Vaerenbergh, X. Sheng, R. Liu, C. Li, Z. Liu, M. Foltin, S. Yu, Q. Xia, et al., Power-efficient combinatorial optimization using intrinsic noise in memristor hopfield neural networks. Nature Electronics **3**(7), 409–418 (2020)
- [5] N. Mohseni, P.L. McMahon, T. Byrnes, Ising machines as hardware solvers of combinatorial optimization problems. Nature Reviews Physics **4**(6), 363–379 (2022)
- [6] T. Wang, L. Wu, P. Nobel, J. Roychowdhury, Solving combinatorial optimisation problems using oscillator based ising machines. Natural Computing **20**(2), 287–306 (2021)

- [7] S. Dutta, A. Khanna, A.S. Assoa, H. Paik, D.G. Schlom, Z. Toroczkai, A. Raychowdhury, S. Datta, An Ising Hamiltonian solver based on coupled stochastic phase-transition nano-oscillators. *Nature Electronics* **4**(7), 502–512 (2021)
- [8] W. Moy, I. Ahmed, P.w. Chiu, J. Moy, S.S. Sapatnekar, C.H. Kim, A 1,968-node coupled ring oscillator circuit for combinatorial optimization problem solving. *Nature Electronics* **5**(5), 310–317 (2022)
- [9] M.W. Johnson, M.H. Amin, S. Gildert, T. Lanting, F. Hamze, N. Dickson, R. Harris, A.J. Berkley, J. Johansson, P. Bunyk, E.M. Chapple, C. Enderud, J.P. Hilton, K. Karimi, E. Ladizinsky, N. Ladizinsky, T. Oh, I. Perminov, C. Rich, M.C. Thom, E. Tolkacheva, C.J. Truncik, S. Uchaikin, J. Wang, B. Wilson, G. Rose, Quantum annealing with manufactured spins. *Nature* **473**(7346), 194–198 (2011)
- [10] R. Barends, A. Shabani, L. Lamata, J. Kelly, A. Mezzacapo, U.L. Heras, R. Babush, A.G. Fowler, B. Campbell, Y. Chen, et al., Digitized adiabatic quantum computing with a superconducting circuit. *Nature* **534**(7606), 222–226 (2016)
- [11] S. Puri, C.K. Andersen, A.L. Grimsmo, A. Blais, Quantum annealing with all-to-all connected nonlinear oscillators. *Nature Communications* **8**(1), 15785 (2017)
- [12] E. Farhi, J. Goldstone, S. Gutmann, J. Lapan, A. Lundgren, D. Preda, A quantum adiabatic evolution algorithm applied to random instances of an NP-complete problem. *Science* **292**(5516), 472–476 (2001)
- [13] N.G. Dickson, M.W. Johnson, M. Amin, R. Harris, F. Altomare, A.J. Berkley, P. Bunyk, J. Cai, E. Chapple, P. Chavez, et al., Thermally assisted quantum annealing of a 16-qubit problem. *Nature Communications* **4**(1), 1903 (2013)
- [14] Y. Zhao, Z. Ma, Z. He, H. Liao, Y.C. Wang, J. Wang, Y. Li, Quantum annealing of a frustrated magnet. *Nature Communications* **15**(1), 3495 (2024)
- [15] S. Tsukamoto, M. Takatsu, S. Matsubara, H. Tamura, An accelerator architecture for combinatorial optimization problems. *Fujitsu Scientific and Technical Journal* **53**(5), 8–13 (2017)
- [16] X. Yin, Y. Qian, A. Vardar, M. Günther, F. Müller, N. Laleni, Z. Zhao, Z. Jiang, Z. Shi, Y. Shi, et al., Ferroelectric compute-in-memory annealer for combinatorial optimization problems. *Nature Communications* **15**(1), 2419 (2024)
- [17] M. Yamaoka, C. Yoshimura, M. Hayashi, T. Okuyama, H. Aoki, H. Mizuno, A 20k-spin Ising chip to solve combinatorial optimization problems with CMOS annealing. *IEEE Journal of Solid-State Circuits* **51**(1), 303–309 (2016)
- [18] N.S. Singh, K. Kobayashi, Q. Cao, K. Selcuk, T. Hu, S. Niazi, N.A. Aadit, S. Kanai, H. Ohno, S. Fukami, et al., Cmos plus stochastic nanomagnets enabling heterogeneous computers for probabilistic inference and learning. *Nature*

- [19] A. Marandi, Z. Wang, K. Takata, R.L. Byer, Y. Yamamoto, Network of time-multiplexed optical parametric oscillators as a coherent Ising machine. *Nature Photonics* **8**(12), 937–942 (2014)
- [20] C. Roques-Carmes, Y. Shen, C. Zancoci, M. Prabhu, F. Atieh, L. Jing, T. Dubček, C. Mao, M.R. Johnson, V. Čeperić, et al., Heuristic recurrent algorithms for photonic ising machines. *Nature Communications* **11**(1), 249 (2020)
- [21] M. Babaeian, D.T. Nguyen, V. Demir, M. Akbulut, P.A. Blanche, Y. Kaneda, S. Guha, M.A. Neifeld, N. Peyghambarian, A single shot coherent ising machine based on a network of injection-locked multicore fiber lasers. *Nature Communications* **10**(1), 3516 (2019)
- [22] S. Kirkpatrick, C.D. Gelatt Jr, M.P. Vecchi, Optimization by simulated annealing. *Science* **220**(4598), 671–680 (1983)
- [23] C.W. Wu, L.O. Chua, Application of graph theory to the synchronization in an array of coupled nonlinear oscillators. *IEEE Transactions on Circuits and Systems I: Fundamental Theory and Applications* **42**(8), 494–497 (1995)
- [24] D. Lee, J. Lee, S. Lee, C. Lee, S. Heo, H. Hwang, Nonvolatile Frequency-Programmable Oscillator With NbO₂ and Li-Based Electro-Chemical Random Access Memory for Coupled Oscillators-Based Temporal Pattern Recognition System. *IEEE Electron Device Letters* **43**(7), 1041–1044 (2022)
- [25] M. Zahedinejad, A.A. Awad, S. Muralidhar, R. Khymyn, H. Fulara, H. Mazraati, M. Dvornik, J. Åkerman, Two-dimensional mutually synchronized spin Hall nano-oscillator arrays for neuromorphic computing. *Nature Nanotechnology* **15**(1), 47–52 (2020)
- [26] A. Mallick, M.K. Bashar, D.S. Truesdell, B.H. Calhoun, S. Joshi, N. Shukla, Using synchronized oscillators to compute the maximum independent set. *Nature Communications* **11**(1) (2020)
- [27] M.K. Bashar, A. Mallick, D.S. Truesdell, B.H. Calhoun, S. Joshi, N. Shukla, Experimental Demonstration of a Reconfigurable Coupled Oscillator Platform to Solve the Max-Cut Problem. *IEEE Journal on Exploratory Solid-State Computational Devices and Circuits* **6**(2), 116–121 (2020)
- [28] I. Ahmed, P.W. Chiu, W. Moy, C.H. Kim, A Probabilistic Compute Fabric Based on Coupled Ring Oscillators for Solving Combinatorial Optimization Problems. *IEEE Journal of Solid-State Circuits* **56**(9), 2870–2880 (2021)
- [29] C.W. Wu, Graph coloring via synchronization of coupled oscillators. *IEEE Transactions on Circuits and Systems I: Fundamental Theory and Applications* **45**(9),

974–978 (1998)

- [30] T. Wang, J. Roychowdhury, *OIM: Oscillator-based Ising machines for solving combinatorial optimisation problems*, in *Unconventional Computation and Natural Computation: 18th International Conference, UCNC 2019, Tokyo, Japan, June 3–7, 2019, Proceedings 18* (Springer, 2019), pp. 232–256
- [31] T. Wang, J. Roychowdhury, *Design tools for oscillator-based computing systems*, in *Proceedings of the 52nd Annual Design Automation Conference* (2015), pp. 1–6
- [32] Y. Kuramoto, *Self-entrainment of a population of coupled non-linear oscillators*, in *International Symposium on Mathematical Problems in Theoretical Physics: January 23–29, 1975, Kyoto University, Kyoto/Japan* (Springer, 1975), pp. 420–422
- [33] M.K. Bashar, Z. Lin, N. Shukla, Stability of oscillator ising machines: Not all solutions are created equal. *Journal of Applied Physics* **134**(14) (2023)
- [34] Y. Cheng, M. Khairul Bashar, N. Shukla, Z. Lin, A control theoretic analysis of oscillator ising machines. *Chaos: An Interdisciplinary Journal of Nonlinear Science* **34** (2024)
- [35] G. Grüner, *Density waves in solids*, vol. 89 (Addison-Wesley, 1994)
- [36] P. Monceau, Electronic crystals: an experimental overview. *Advances in Physics* **61**(4), 325–581 (2012)
- [37] S.V. Zaitsev-Zotov, Finite-size effects in quasi-one-dimensional conductors with a charge-density wave. *Physics-Uspekhi* **47**(6), 533 (2004)
- [38] A.A. Balandin, S.V. Zaitsev-Zotov, G. Grüner, Charge-density-wave quantum materials and devices—new developments and future prospects. *Applied Physics Letters* **119**(17), 170401 (2021)
- [39] J. Bardeen, Theory of non-ohmic conduction from charge-density waves in nbse3. *Phys. Rev. Lett.* **42**(22), 1498 (1979)
- [40] D.S. Fisher, Sliding charge-density waves as a dynamic critical phenomenon. *Phys. Rev. Lett.* **50**(19), 1486 (1983)
- [41] D.S. Fisher, Collective transport in random media: from superconductors to earthquakes. *J. Phys. IV France* **131**, 89–94 (2005)
- [42] S.V. Zaitsev-Zotov, Classical-to-quantum crossover in charge-density wave creep at low temperatures. *Phys. Rev. Lett.* **71**(4), 606 (1993)
- [43] I.A. Cohn, S.V. Zaitsev-Zotov, Magnetic field induced activated and quantum creep of charge density waves in o-tas3. *Phys. Rev. B* **108**(11), 115124 (2023)

- [44] Y.I. Latyshev, Aharonov-bohm effect on charge density wave (cdw) moving through columnar defects in nbse₃. Phys. Rev. Lett. **78**(5), 919 (1997)
- [45] H. Matsukawa, Charge density wave dynamics in quasi-one-dimensional conductors. J. Phys. IV France **9**, 10–161 (1999)
- [46] S. Zybtev, V. Pokrovskii, S. Zaitsev-Zotov, 'quantized' states of the charge-density wave in microcrystals of K_{0.3}MoO₃. Nat. Commun. **1**, 85 (2010)
- [47] J.S. Miller Jr., A. Wijesinghe, Z. Tang, A.M. Guloy, Pressure-induced superconductivity in the charge-density-wave compound rbfese₂. Phys. Rev. Lett. **108**(3), 036404 (2012)
- [48] J.S. Miller Jr., A. Wijesinghe, Z. Tang, A.M. Guloy, Unusual electronic transport in rbfese₂ under pressure. Phys. Rev. B **87**(11), 115127 (2013)
- [49] J.O. Brown, M. Taheri, F. Kargar, R. Salgado, T. Geremew, S. Rumyantsev, R.K. Lake, A.A. Balandin, Current fluctuations and domain depinning in quasi-two-dimensional charge-density-wave 1T-TaS₂ thin films. Applied Physics Reviews **10**(4) (2023)
- [50] M. Taheri, J. Brown, A. Rehman, N. Sesing, F. Kargar, T.T. Salguero, S. Rumyantsev, A.A. Balandin, Electrical Gating of the Charge-Density-Wave Phases in Two-Dimensional h-BN/1T-TaS₂ Devices. ACS Nano **16**(11), 18968–18977 (2022)
- [51] M. Taheri, N. Sesing, T.T. Salguero, A.A. Balandin, Electric-field modulation of the charge-density-wave quantum condensate in h-BN/NbS₃ quasi-2D/1D heterostructure devices. Applied Physics Letters **123**(23) (2023)
- [52] A.H. Thompson, R.F. Gamble, J.F. Revelli, Transitions between semiconducting and metallic phases in 1T-TaS₂. Solid State Communications **9**(13), 981–985 (1971)
- [53] R. Manzke, T. Buslaps, B. Pfalzgraf, M. Skibowski, O. Anderson, On the Phase Transitions in 1T-TaS₂. Europhysics Letters **8**(2), 195–200 (1989)
- [54] G. Liu, B. Debnath, T.R. Pope, T.T. Salguero, R.K. Lake, A.A. Balandin, A charge-density-wave oscillator based on an integrated tantalum disulfide-boron nitride-graphene device operating at room temperature. Nature Nanotechnology **11**(10), 845–850 (2016)
- [55] C. Butler, M. Yoshida, T. Hanaguri, Y. Iwasa, Mottness versus unit-cell doubling as the driver of the insulating state in 1T-TaS₂. Nature Communications **11**(1), 2477 (2020)

- [56] A. Mohammadzadeh, S. Baraghani, S. Yin, F. Kargar, J.P. Bird, A.A. Balandin, Evidence for a thermally driven charge-density-wave transition in 1T-TaS₂ thin-film devices: Prospects for GHz switching speed. *Applied Physics Letters* **118**(9), 093102 (2021)
- [57] Y. Yu, F. Yang, X.F. Lu, Y.J. Yan, Y.H. Cho, L. Ma, X. Niu, S. Kim, Y.W. Son, D. Feng, et al., Gate-tunable phase transitions in thin flakes of 1T-TaS₂. *Nature Nanotechnology* **10**(3), 270–276 (2015)
- [58] B. Sipos, A.F. Kusmartseva, A. Akrap, H. Berger, L. Forró, E. Tutiš, From mott state to superconductivity in 1T-TaS₂. *Nature Materials* **7**(12), 960–965 (2008)
- [59] A.K. Geremew, F. Kargar, E. Zhang, S. Zhao, E. Aytan, M. Bloodgood, T.T. Salguero, S. Rumyantsev, A. Fedoseyev, D. Fleetwood, et al., Proton-irradiation-immune electronics implemented with two-dimensional charge-density-wave devices. *Nanoscale* **11**(17), 8380–8386 (2019)
- [60] L. Stojchevska, I. Vaskivskiy, T. Mertelj, P. Kusar, D. Svetin, S. Brazovskii, D. Mihailovic, Ultrafast switching to a stable hidden quantum state in an electronic crystal. *Science* **344**(6180), 177–180 (2014)
- [61] J. Ravnik, M. Diego, Y. Gerasimenko, Y. Vaskivskiy, I. Vaskivskiy, T. Mertelj, J. Vodeb, D. Mihailovic, A time-domain phase diagram of metastable states in a charge ordered quantum material. *Nature Communications* **12**(1) (2021)
- [62] A. Mraz, Venturini, et al., Charge Configuration Memory Devices: Energy Efficiency and Switching Speed **41**, 3 (2022)
- [63] C. Zhu, Y. Chen, F. Liu, S. Zheng, X. Li, A. Chaturvedi, J. Zhou, Q. Fu, Y. He, Q. Zeng, et al., Light-tunable 1T-TaS₂ charge-density-wave oscillators. *ACS nano* **12**(11), 11203–11210 (2018)
- [64] Y. Wang, W. Yao, Z. Xin, T. Han, Z. Wang, L. Chen, C. Cai, Y. Li, Y. Zhang, Band insulator to mott insulator transition in 1 t-tas2. *Nature communications* **11**(1), 4215 (2020)
- [65] M. Yoshida, Y. Zhang, J. Ye, R. Suzuki, Y. Imai, S. Kimura, A. Fujiwara, Y. Iwasa, Controlling charge-density-wave states in nano-thick crystals of 1T-TaS₂. *Sci. Reports* **4**(1), 1–5 (2014)
- [66] M. Yoshida, R. Suzuki, Y. Zhang, M. Nakano, Y. Iwasa, Memristive phase switching in two-dimensional 1t-tas2 crystals. *Science advances* **1**(9), e1500606 (2015)
- [67] H. Nakao, Phase reduction approach to synchronisation of nonlinear oscillators. *Contemporary Physics* **57**(2), 188–214 (2016)

- [68] A. Lucas, Ising formulations of many np problems. *Frontiers in physics* **2**, 5 (2014)
- [69] A. Todri-Sanial, et al., How frequency injection locking can train oscillatory neural networks to compute in phase. *IEEE transactions on neural networks and learning systems* **33**(5), 1996–2009 (2021)
- [70] A. Neogy, J. Roychowdhury, *Analysis and design of sub-harmonically injection locked oscillators*, in *2012 Design, Automation & Test in Europe Conference & Exhibition (DATE)* (IEEE, 2012), pp. 1209–1214
- [71] P. Bhansali, J. Roychowdhury, *Gen-Adler: The generalized Adler’s equation for injection locking analysis in oscillators*, in *2009 Asia and South Pacific Design Automation Conference* (IEEE, 2009), pp. 522–527
- [72] C.A. Floudas, P.M. Pardalos, *Encyclopedia of optimization* (Springer Science & Business Media, 2008)
- [73] M. Binnewies, R. Glaum, M. Schmidt, P. Schmidt, Chemical Vapor Transport Reactions – A Historical Review. *Zeitschrift für anorganische und allgemeine Chemie* **639**(2), 219–229 (2013)
- [74] J.A. Acebrón, L.L. Bonilla, C.J. Pérez Vicente, F. Ritort, R. Spigler, The kuramoto model: A simple paradigm for synchronization phenomena. *Reviews of modern physics* **77**(1), 137–185 (2005)
- [75] T. Wang, J. Roychowdhury, *PHLOGON: Phase-based logic using oscillatory nano-systems*, in *Unconventional Computation and Natural Computation: 13th International Conference, UCNC 2014, London, ON, Canada, July 14-18, 2014, Proceedings 13* (Springer, 2014), pp. 353–366
- [76] H. Lo, W. Moy, H. Yu, S. Sapatnekar, C.H. Kim, An ising solver chip based on coupled ring oscillators with a 48-node all-to-all connected array architecture. *Nature Electronics* **6**(10), 771–778 (2023)
- [77] M.J. Avedillo, et al., Operating coupled vo 2-based oscillators for solving ising models. *IEEE Journal on Emerging and Selected Topics in Circuits and Systems* (2023)
- [78] M.S. Mian, K. Okimura, J. Sakai, Self-oscillation up to 9 MHz based on voltage triggered switching in VO₂/TiN point contact junctions. *Journal of Applied Physics* **117**(21) (2015)
- [79] E. Corti, B. Gotsmann, K. Moselund, A.M. Ionescu, J. Robertson, S. Karg, Scaled resistively-coupled VO₂ oscillators for neuromorphic computing. *Solid-State Electronics* **168**, 107729 (2020)

- [80] S. Carapezzi, A. Plews, G. Boschetto, A. Nejim, S. Karg, A. Todri-Sanial, How fast can vanadium dioxide neuron-mimicking devices oscillate? Physical mechanisms limiting the frequency of vanadium dioxide oscillators. *Neuromorphic Computing and Engineering* **3**(3), 034010 (2023)
- [81] E. Corti, A. Khanna, K. Niang, J. Robertson, K.E. Moselund, B. Gotsmann, S. Datta, S. Karg, Time-Delay Encoded Image Recognition in a Network of Resistively Coupled VO₂ on Si Oscillators. *IEEE Electron Device Letters* **41**(4), 629–632 (2020)
- [82] F.C. Hoppensteadt, E.M. Izhikevich, Pattern recognition via synchronization in phase-locked loop neural networks. *IEEE Transactions on Neural Networks* **11**(3), 734–738 (2000)
- [83] C. Delacour, S. Carapezzi, M. Abernot, A. Todri-Sanial, Energy-Performance Assessment of Oscillatory Neural Networks Based on VO₂ Devices for Future Edge AI Computing. *IEEE Transactions on Neural Networks and Learning Systems* pp. 1–14 (2023)
- [84] S.S. Rathod, A.K. Saxena, S. Dasgupta, Radiation effects in MOS-based devices and circuits: A review. *IETE Technical Review (Institution of Electronics and Telecommunication Engineers, India)* **28**(6), 451–469 (2011)
- [85] A.S. Keys, J.H. Adams, J.D. Cressler, R.C. Darty, M.A. Johnson, M.C. Patrick, High-performance, radiation-hardened electronics for space and lunar environments. *AIP Conference Proceedings* **969**, 749–756 (2008)
- [86] M.G. Buehler, B.R. Blaes, Y.S. Lin, Radiation dependence of inverter propagation delay from timing sampler measurements. *IEEE Transactions on Nuclear Science* **36**(6), 1981–1989 (1989)
- [87] G. Liu, E. Zhang, C. Liang, M. Bloodgood, T.T. Salguero, D. Fleetwood, A.A. Balandin, Total-ionizing-dose effects on threshold switching in 1T-TaS₂ charge density wave devices. *IEEE Electron Device Letters* **38**(12), 1724–1727 (2017)
- [88] D.J. Frank, R.H. Dennard, E. Nowak, P.M. Solomon, Y. Taur, H.S.P. Wong, Device scaling limits of Si MOSFETs and their application dependencies. *Proceedings of the IEEE* **89**(3), 259–287 (2001)
- [89] F.J. Morin, Oxides which show a metal-to-insulator transition at the neel temperature. *Physical Review Letters* **3**, 34–36 (1959)